

Investigation of Bubble-Slag Layer Behaviors with Hybrid Eulerian–Lagrangian Modeling and Large Eddy Simulation

LINMIN LI¹ and BAOKUAN LI^{1,2}

1.—School of Materials and Metallurgy, Northeastern University, Shenyang 110819, People's Republic of China. 2.—e-mail: libk@smm.neu.edu.cn

In ladle metallurgy, bubble–liquid interaction leads to complex phase structures. Gas bubble behavior, as well as the induced slag layer behavior, plays a significant role in the refining process and the steel quality. In the present work, a mathematical model using the large eddy simulation (LES) is developed to investigate the bubble transport and slag layer behavior in a water model of an argon-stirred ladle. The Eulerian volume of fluid model is adopted to track the liquid steel–slag–air free surfaces while the Lagrangian discrete phase model is used for tracking and handling the dynamics of discrete bubbles. The bubble coalescence is considered using O'Rourke's algorithm to solve the bubble diameter redistribution and bubbles are removed after leaving the air–liquid interface. The turbulent liquid flow that is induced by bubble–liquid interaction is solved by LES. The slag layer fluctuation, slag droplet entrainment and spout eye open–close phenomenon are well revealed. The bubble diameter distribution and the spout eye size are compared with the experiment. The results show that the hybrid Eulerian–Lagrangian–LES model provides a valid modeling framework to predict the unsteady gas bubble–slag layer coupled behaviors.

List of Symbols

b_{cri}	Criteria impact parameter (m)
C_D	Drag force coefficient
C_{VM}	Virtual mass force coefficient
C_L	Lift force coefficient
C_S	Smagorinsky constant
d	Distance to the closest wall (m)
d_{pi}	Initial bubble diameter (m)
F_{VM}	Virtual mass force (m/s^2)
F_L	Lift force (m/s^2)
F_{PG}	Pressure gradient force (m/s^2)
g	Gravitational acceleration (m/s^2)
n	Number of bubbles
P	Pressure (Pa)
Q	Gas flow rate (m^3/s)
r	Bubble radii (m)
Re	Relative Reynolds Number
S	Rate-of-strain tensor (s^{-1})
t	Time (s)
u	Velocity (m/s)
V	Cell volume (m^3)
We	Collisional Weber number

τ	Subgrid-scale stress (N/m^2)
μ	Viscosity (kg/m/s)
μ_t	Turbulent viscosity (kg/m/s)
κ	Von Kármán constant
δ_{ij}	Dirac function

INTRODUCTION

Argon gas stirring is widely employed in steel refining processes to homogenize the chemical composition of alloy elements and temperature. Discrete gas bubbles that injected through porous plug(s) help to remove inclusions and to enhance the rates of refining reactions when they float, entrain the surrounding molten steel into their wakes, and break up the slag layer. The discrete bubbles go up desultorily, possibly aggregate with each other, and form a turbulent bubble plume. At a high gas flow rate, it is insufficient for the inverse flow to close the spout eye and a quasi-steady condition is achieved to form a large spout eye, which causes the exposure of molten steel. Strong stirring is needed to promote the efficiency of desulfurization and slag/steel intermixing.

Greek Letters

α	Volume fraction
ρ	Density (kg/m^3)
σ	Stress tensor (N/m^2)

But a large open eye is undesirable in order to avoid the pick-up of oxygen and nitrogen, the entrainment of slag, and the generation of exogenous inclusions from refractory wear. On the other hand, a calm flow with small bubbles is needed for inclusion removal. Figure 1 shows the top free surface and the spout eye in a real ladle inside of which is almost impossible to investigate the flow and transmission. As mentioned by Nastac,¹ the application of CFD in the manufacturing industry often leads to shortened design and improved process performance. Therefore, a comprehensive model, depicting the multi-phase flow pattern with bubble–liquid interactions and interfacial behaviors, is helpful to understand the mechanisms of the various phenomena inside the ladle (e.g., mixing, slag emulsification, exogenous inclusion generation) and improve the refining performance.

The interaction between the discrete bubbles and continuous multi-fluids is one of the most crucial shortcomings of current multi-fluid models. Zheng and Yu² described the long-standing challenge in granular dynamics modeling and explained the issues for continuum theories to describe the granular materials. Currently, numbers of mathematical models have been proposed to investigate the flow characteristic and slag layer behavior in the gas-stirred ladle. Both the Eulerian approach^{3–8} and the Lagrangian approach^{9–15} were used to deal with the gas bubble phase. The results of Klostermann et al.¹⁶ showed that the volume of fluid method (VOF)¹⁷ is suitable for rising bubble problems where the bubbles are much larger than the grid size. Zhang et al.¹⁸ introduced the two main approaches to model the behavior of second-phase particles and proposed a well-revealed air bubble motion and surface fluctuation results with the VOF model. In fact, as was found in the experiments,^{7,10} the bubbles injected by porous plug(s) are dispersed in the ladle. This makes it difficult to model the discrete bubbles in an Eulerian way. The population balance model (PBM), which provides a valid method for the bubble diameter prediction, has been recently adopted in several works,^{4,7,8} but still lacks the description of bubble–bubble and bubble–liquid interactions. Johansen and Boysan⁹ and Guo and Irons¹⁰ proposed an Eulerian–Lagrangian formulation for the gas–liquid flow in the ladle without considering the slag layer. Liu et al.¹¹ employed the Lagrangian approach and the Eulerian VOF model to track the bubbles and the free surfaces respectively, but the unsteady slag layer behavior was not discussed and the bubble diameter redistribution was not considered. Recently, Thomas's group^{13,14} coupled the large eddy simulation and discrete phase model to study the transient flow during the continuous casting of steel slabs and revealed good velocity fluctuation results. Li et al.¹⁵ studied the unsteady slag layer behavior by modeling the bubble phase in the Lagrangian way and using the large eddy simulation, but the bubble aggregation and breakage were ignored. Recently, several

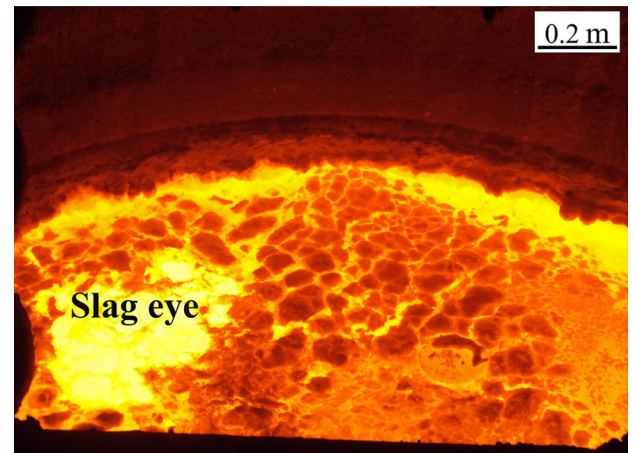


Fig. 1. The top free surface and slag eye in a real ladle.

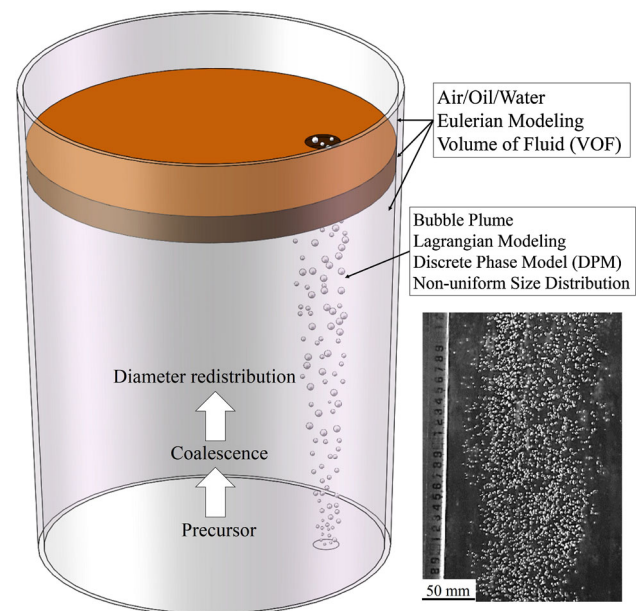


Fig. 2. Schematic gas-stirring process, gas distribution in water model and calculation approaches for different phases.

reports^{19–21} have shown that a Lagrangian description for bubbles is appropriate to model the discrete bubble behaviors and the gas–liquid interactions.

On the other hand, from the observation of the slag layer fluctuation and the spout eye formation, a transient complex turbulent multiphase phenomenon has been found. A large number of eddies with a wide range of length and time scales exist in the bath. This is closely related to the phenomena of slag layer break up, fluctuation and slag droplet entrainment. Previous simulations were always based on the Reynolds-averaged Navier–Stokes (RANS) equations, and it is hard for these models to describe the above-mentioned unsteady phenomena. The large eddy simulation (LES) resolves large eddies directly while small eddies are modeled using the subgrid scale (SGS) model, and these have been

successfully taken into industrial applications^{13–15,22} indicating that the LES model is available to obtain detailed turbulent flow structures. The present work tracks the bubbles using the discrete phase model (DPM). The bubble coalescence, going through the slag layer, and the removal at the top surface are simulated. Importantly, the present work uses O'Rourke's algorithm to solve the bubble diameter redistribution. It is an improvement on the previous work¹⁵ which ignored the bubble nonuniform size distribution. The free surfaces among the liquid steel, slag and air are tracked using the VOF model. The multiphase (liquid steel, slag, air and bubble phases) turbulent flow is simulated using the LES with the Smagorinsky SGS model to describe the complex phase structures. The diagrammatic sketch of gas bubble stirring process and the calculation approaches for different phases are shown in Fig. 2.

MODEL DESCRIPTION

There are two basic formulation schemes for the simulations: the Eulerian–Eulerian formulation and the Eulerian–Lagrangian formulation. As mentioned above, the bubbles are dispersed in the ladle with a small volume fraction while the molten steel and slag are continuous. The present model treats the liquid phases in a fixed or Eulerian frame of reference, similar to a single phase calculation, while the bubble phase equations are solved in a Lagrangian frame of reference. The gas bubble velocity and the void fraction are obtained by tracking a large number of bubbles and averaging. Because the phases are computed in different references, the forces between the bubble phase and the continuous phases, the momentum transport, are vitally important. In this work, the buoyancy, drag force, virtual mass force, lift force and pressure gradient force are calculated and transported from bubble phase to liquid phases. The bubbles will disappear and join to the air to be a continuum after coming through the slag layer, so the present model removes the bubbles when they arrive the position where the air volume fraction is 0.5.

VOF AND LES

The VOF model can model two or more immiscible fluids and it has been adopted for tracking the interfaces. The interface reconstruction is the most crucial part in the model and is carried out with the help of geometric advection. An elaborate description of the complete VOF model can be found in van Sint Annaland et al.²³ The tracking of the interfaces is accomplished by the solution of a continuity equation for the volume fraction. For the q th phase, the continuity equation is described in the following form:

$$\frac{\partial \alpha_q}{\partial t} + \frac{\partial}{\partial x_i} (\alpha_q u_i) = 0, \quad (1)$$

where the volume fraction α_q is constrained by $\sum_{q=1}^n \alpha_q = 1$, and u represents the velocity. In the VOF model, it is assumed that the velocity field is shared among the phases and a single momentum equation is solved throughout the domain. The LES model is the widely known scale-resolving simulation (SRS) model which resolves large turbulent structures in space and time down to the grid limit everywhere in the flow. The governing equations employed for LES are obtained by filtering the time-dependent Navier–Stokes equations. The filtering process effectively filters out the eddies that are smaller than the filter width or grid spacing used in the calculations. The filtered Navier–Stokes equation can be described as:

$$\frac{\partial(\rho \bar{u}_i)}{\partial t} + \frac{\partial(\rho \bar{u}_i \bar{u}_j)}{\partial x_j} = -\frac{\partial \bar{P}}{\partial x_i} + \frac{\partial}{\partial x_j} (\sigma_{ij}) - \frac{\partial \tau_{ij}}{\partial x_j} + \rho g_i + F_p, \quad (2)$$

Table I. Parameters of the simulation

Parameters	Values
Bottom diameter	617 mm
Slope angle	2.44°
Water depth	700 mm
Slag layer thickness	50 mm
Porous plug diameter	44 mm
Plug radial position	0.67 R
Water density	1000 kg/m
Water viscosity	0.001 kg/m/s
Oil density	890 kg/m ³
Oil viscosity	0.006 kg/m/s
Gas density	1.138 kg/m ³ (25°C)
Gas viscosity	1.663 × 10 ⁻⁵ kg/m/s
Initial bubble diameter	1 mm

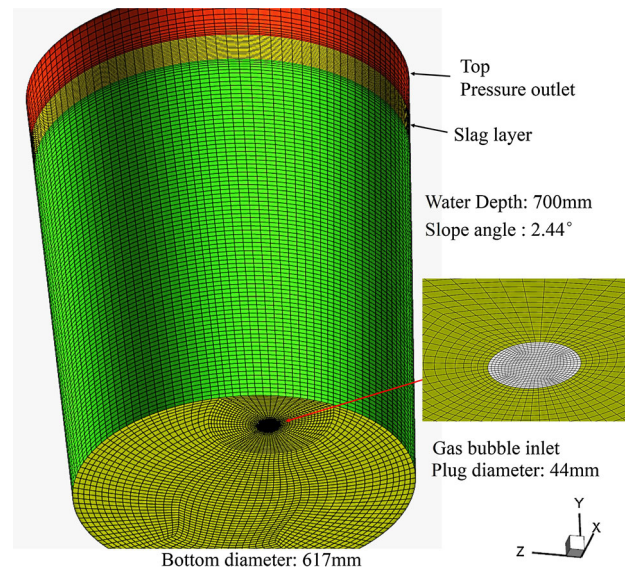


Fig. 3. The geometry size, mesh and boundary conditions.

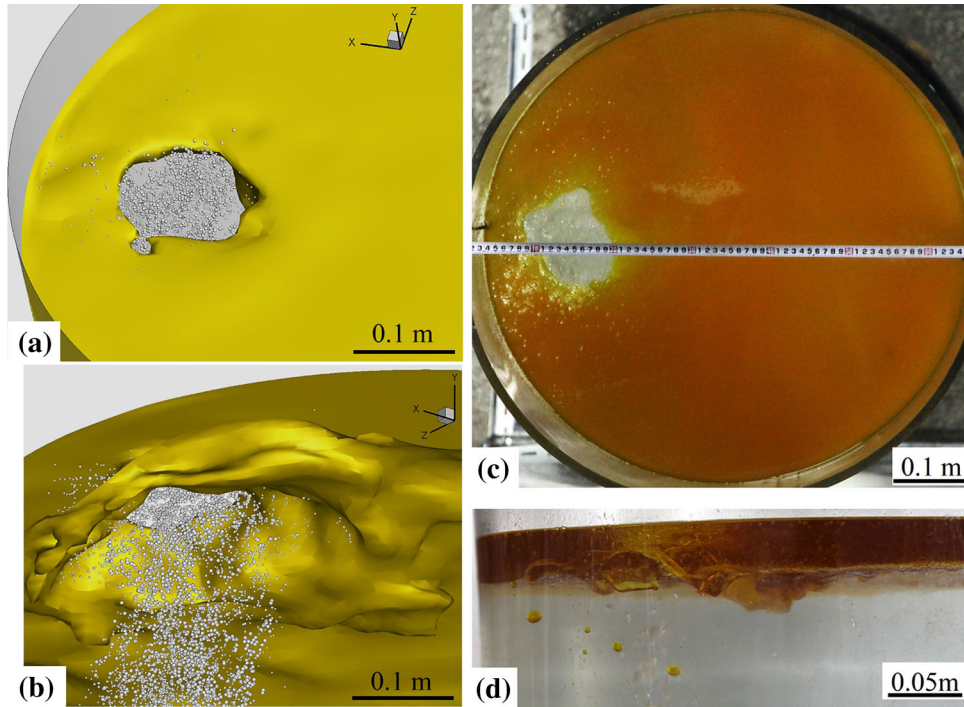


Fig. 4. Slag layer patterns of (a and b) calculation and (c and d) experiment.

where the properties used above are mixture properties. σ_{ij} is the stress tensor, P is the pressure, g_i is the gravitational acceleration if i represents the gravity direction and F_p represents the forces of the bubbles acting on the liquid. τ_{ij} is the sub-grid scale (SGS) stress defined by:

$$\tau_{ij} = \rho(\overline{u_i u_j} - \bar{u}_i \bar{u}_j). \quad (3)$$

The SGS stress resulting from the filtering operation is modeled using the form²⁴ as:

$$\tau_{ij} - \frac{1}{3} \tau_{kk} \delta_{ij} = -2\mu_t \bar{S}_{ij}, \quad (4)$$

where μ_t is the SGS turbulent viscosity, δ_{ij} is equal to 1 if $i = j$, and 0 otherwise. \bar{S}_{ij} is the rate-of-strain tensor for the resolved scale that is defined by:

$$\bar{S}_{ij} = \frac{1}{2} \left(\frac{\partial \bar{u}_i}{\partial x_j} + \frac{\partial \bar{u}_j}{\partial x_i} \right). \quad (5)$$

The eddy viscosity is calculated as:

$$\mu_t = \rho \left(\min(\kappa d, C_S V^{1/3}) \right)^2 \sqrt{2\bar{S}_{ij} \bar{S}_{ij}}, \quad (6)$$

where κ is the von Kármán constant set as 0.4, d is the distance to the closest wall, V is the volume of the computational cell and C_S is the Smagorinsky constant equal to 0.1.

Discrete Phase Model

The trajectory of each bubble is simulated by integrating the force balance on it which is written in a Lagrangian reference frame. The motion for

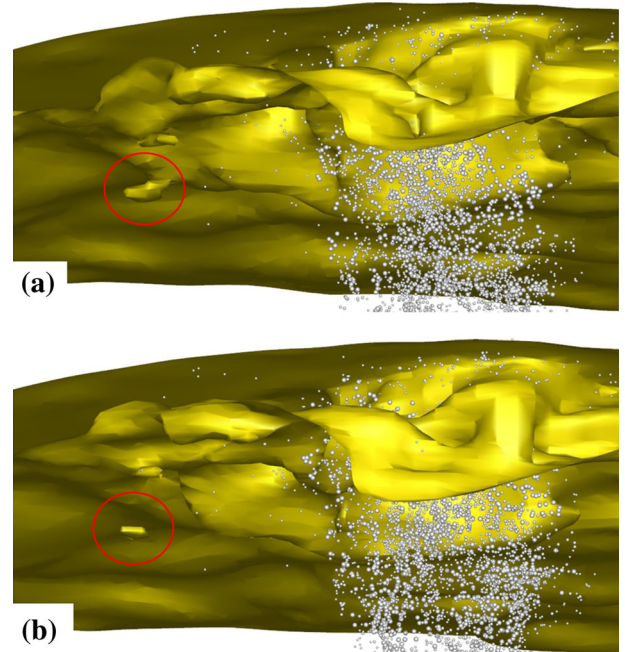


Fig. 5. Slag droplet entrainment phenomenon in calculation: (a) before and (b) after entrainment.

each individual bubble is calculated from Newton's second law. The liquid phase contributions are taken into account via the forces experienced by each individual bubble. For an incompressible bubble, the momentum equation can be described as:

$$\frac{d\vec{u}_p}{dt} = F_D(\vec{u} - \vec{u}_p) + \frac{\vec{g}(\rho_p - \rho)}{\rho_p} + \vec{F}_{VM} + \vec{F}_L + \vec{F}_{PG}, \quad (7)$$

where $F_D(\vec{u} - \vec{u}_p)$ is the drag force per unit bubble mass and F_D is written as:

$$F_D = \frac{18\mu C_D Re}{\rho_p d_p^2 24}, \quad (8)$$

where d_p is the bubble diameter and Re is the relative Reynolds number. In this work, the bubbles are assumed to be spherical throughout the domain and the drag coefficient C_D is calculated as in Morsi and Alexander.²⁵ The additional acceleration terms include the virtual mass force, lift force and pressure gradient force. They can be described as follows:

$$\vec{F}_{VM} = -C_{VM} \frac{\rho}{\rho_p} \left(\vec{u}_p \nabla \vec{u} - \frac{d\vec{u}_p}{dt} \right) \quad (9)$$

$$\vec{F}_L = -C_L \frac{\rho}{\rho_p} \alpha_p (\vec{u} - \vec{u}_p) \times (\nabla \times \vec{u}) \quad (10)$$

$$\vec{F}_{PG} = -\frac{\rho}{\rho_p} \vec{u}_p \nabla \vec{u}, \quad (11)$$

where C_{VM} is the virtual mass factor with a value of 0.5. C_L used in the present study is obtained from Tomiyama et al.²⁶ Detailed discussion about these forces can be found in Darmana et al.²⁷

Coalescence Model

The present work considers the bubble coalescence but ignores the bubble breakage because it is found that, in the present conditions, bubbles are

small and few bubbles break up when going up in the water model. For the description of the coalescence process, O'Rourke's algorithm²⁸ is used. Bubbles are considered to coalesce or bounce by comparing the actual collision parameter and the critical offset, which is a function of the collisional Weber number and the relative radii of the collector (r_1) and the smaller (r_2) one:^{29,30}

$$b_{cri} = (r_1 + r_2) \sqrt{\min\left(1.0, \frac{2.4f}{We}\right)}, \quad (12)$$

where f is a function of r_1/r_2 defined as:

$$f(r_1/r_2) = (r_1/r_2)^3 - 2.4(r_1/r_2)^2 + 2.7(r_1/r_2). \quad (13)$$

NUMERICAL DETAILS

The simulations are performed for a one-third-scale water model that is established with a camera observing the slag open eye and a high speed camera capturing the bubbles. The N_2 (25°C, 1 atm) gas is injected into the liquid from a nozzle made by the porous mullite which is the same as that in the real ladle. The water and oil are used to simulate the molten steel and the slag layer, respectively. The details of the geometric parameters and material properties are shown in Table I.

The computations are performed using the commercial CFD software FLUENT. The grid densities of the 3D all-hexahedral element mesh are determined as follows: the mesh size of the slag layer is set to 3 mm, and the mesh size of the inlet is set to 2 mm. The maximum mesh size of 10 mm and a stretching ratio of 1.1 is used. The mesh and boundary conditions are shown in Fig. 3. The number of total cells is about 500,000.

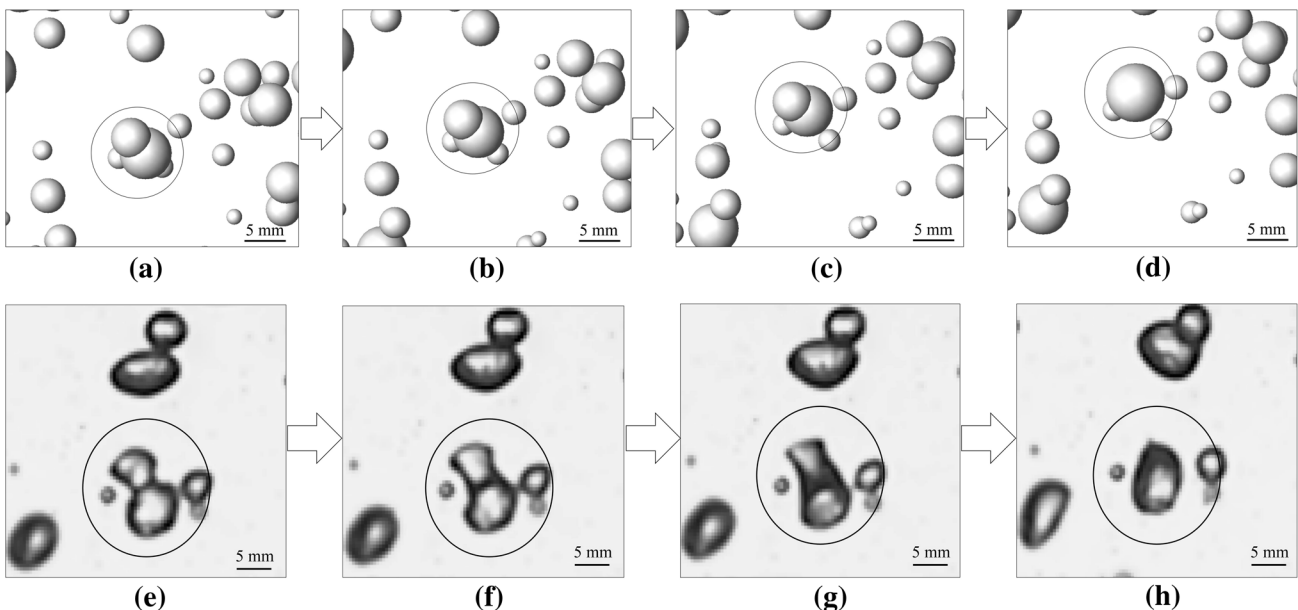


Fig. 6. Bubble coalescence process found in (a–d) calculation and observed in (e–h) experiment.

The calculations are carried out by the transient pressure-based solver. The bounded second-order implicit transient formulation and the bounded central-differencing scheme for momentum are used. The conservation equations are discretized using the control volume technique and the PISO scheme is used for the pressure–velocity coupling. A physical time scale of 0.005 s is adopted. The gas flow rate and the initial bubble diameter are determined according to the experimental measurement. The initial bubble is assumed to be 1 mm as the diameter of the smallest bubbles observed in the bath is about 1 mm. The number of injected bubbles per unit time is calculated according to the gas flow rate and the initial diameter:

$$n = \frac{6Q}{\pi d_{pi}^3}, \quad (14)$$

where Q is the gas flow rate and d_{pi} is the initial bubble diameter.

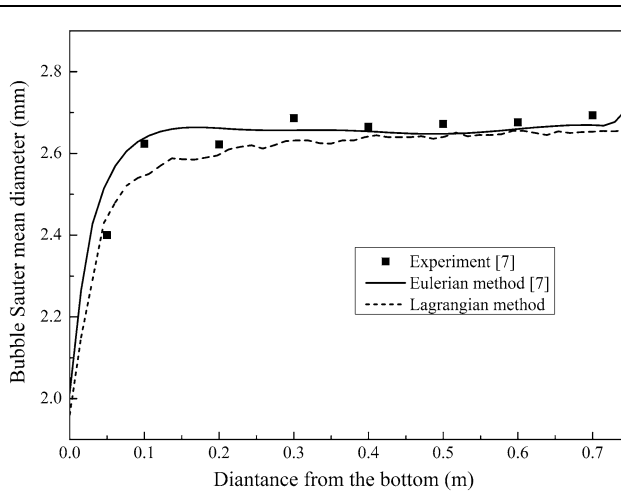


Fig. 7. Bubble Sauter mean diameter at the plume center line along the distance from the bottom.

RESULTS AND DISCUSSION

Slag Layer Fluctuation and Slag-Droplet Entrainment

It is very important to understand the slag layer behavior as it plays a significant role in the ladle metallurgy and steel quality. Figure 4 shows the top surface and the water–oil interface of both calculation and experiment. The simulated interface is displayed using the iso-surface ($\alpha_{oil} = 0.5$). The gas flow rate is 90 L/h, which is relatively high, and a large spout eye forms. It is observed that the top free surface stays much calmer than the water–oil interface. Because the density difference between oil and air is much larger than that between oil and water, it is easier for the top surface to become horizontal. On the other hand, the bubbles transport in chaos and come through the slag layer, cause turbulence with multi-scale eddies, and make the slag layer fluctuate when eddies transport to the periphery of the ladle. Some slag droplets will be dragged down from the continuous layer with the effect of shear stress when the water is coming down. The slag droplet entrainment is also simulated by the current model as shown in Fig. 5. It shows two different times of before (Fig. 5a) and after (Fig. 5b) entrainment. Most of the droplets will float back to the layer while some small droplets will stay for a long time. It is very important to investigate the transport of droplets in the ladle. The present work provides a valid modeling framework to simulate the entrainment phenomenon and help understand the mechanism. Additionally, the present mesh for the calculations is not very fine, so the interface is not very smooth. It is better to draw a finer mesh in the future work for the slag droplet entrainment investigation.

Bubble Coalescence and Diameter Distribution

A high-speed camera is used to capture the bubbles in the water model experiment so that it is available to observe the bubble behavior including

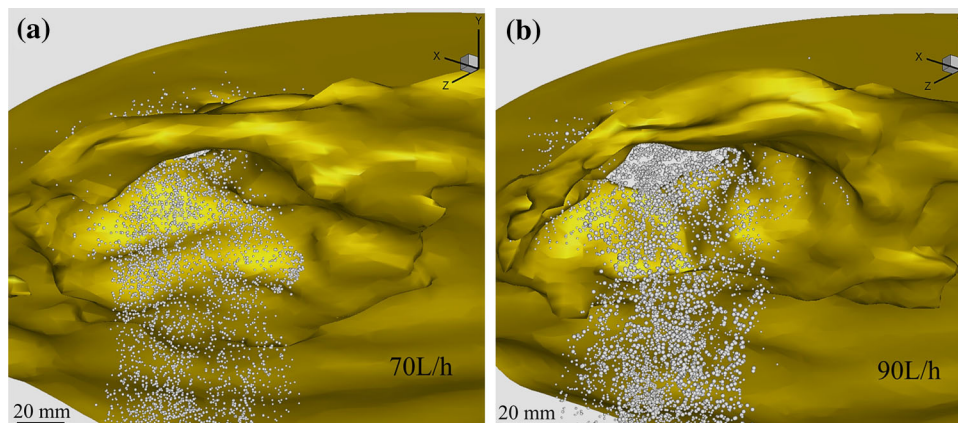


Fig. 8. Slag layer patterns of different gas flow rates: (a) 70 L/h, (b) 90 L/h.

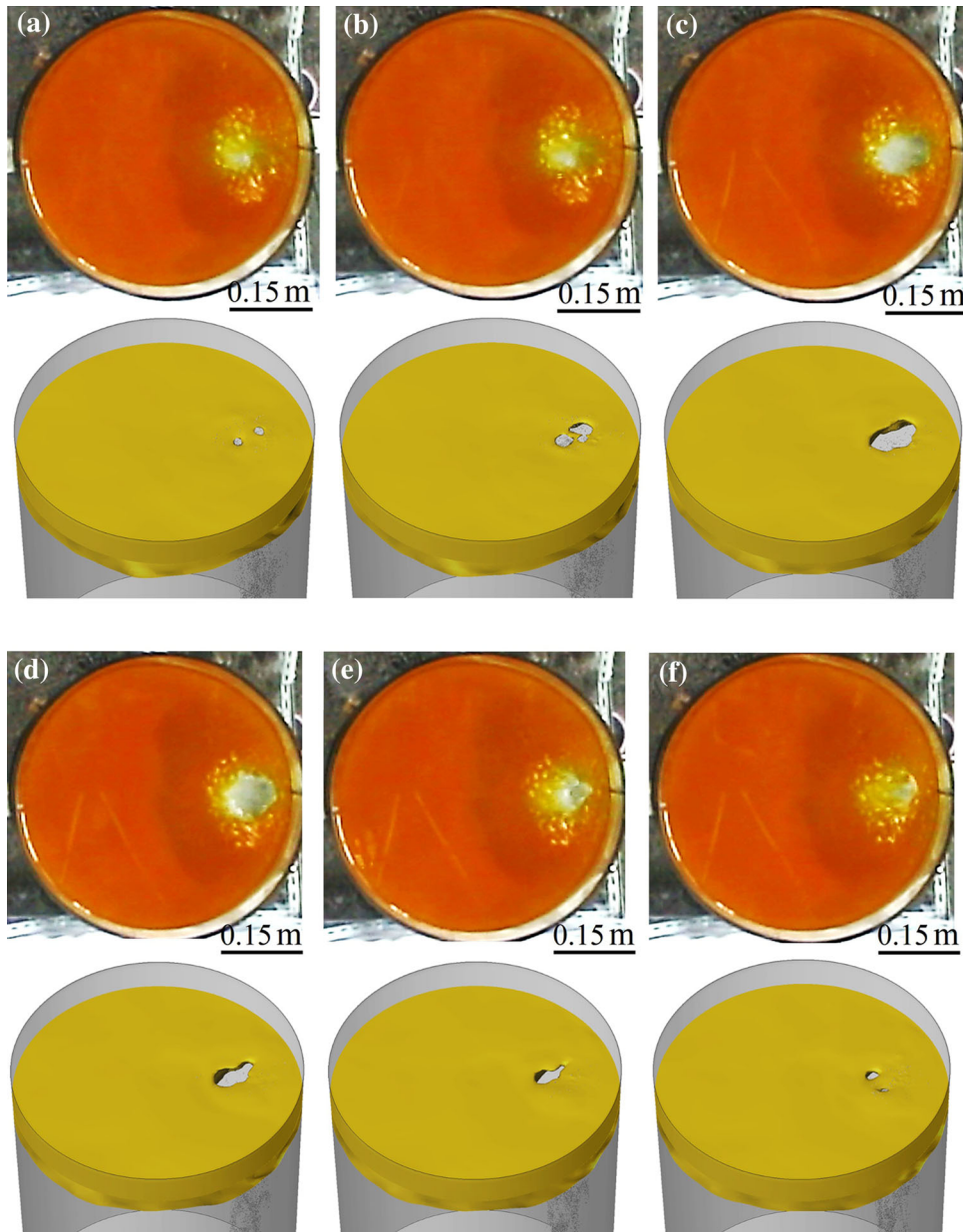


Fig. 9. Slag eye open (a–c) and collapse (d–f) processes of both experiment and simulation.

bubble coalescence and breakage. As is observed, bubbles become quite dispersed when going upward, as shown in Fig. 2, rarely coalesce and break in the bubble plume, except that they just come out from the porous plug in the lower part where the coalescence rate is high. Figure 6 compares the simulated bubble coalescence process with the captured coalescence process in the bubble plume. It shows the procedure that the two bubbles touch each other and coalesce into one larger bubble. The volume of the large bubble is the sum of the volume of the two small bubbles. A

previous work⁷ has reported the bubble diameter distribution in the center line of the bubble plume along with the distance from the bottom. To compare the present predicted bubble diameter redistribution with that, the time average bubble Sauter mean diameter at 50 points of the center line is recorded. Figure 7 compares the bubble diameter distribution of the experiment with that predicted by the two methods for bubble simulation. The result shows good agreement, and it is found that bubble diameter grows much faster in the lower part where the coalescence rate is

higher. After bubbles come out of the aggregation region, they become more dispersed and the diameter changes little. The results show that the present model can predict a quite accurate bubble diameter distribution, and moreover can look

inside the bubble coalescence process and the trajectory of each bubble.

Slag Eye Open–Close Appearance with a Small Gas Flow Rate

The gas flow rate will significantly influence the interface fluctuation and the spout eye formation. In the actual ladle metallurgy, a calm flow and fine bubbles are needed for inclusion removal. It is found that the spout eye appears to open and close repetitively with a small gas flow rate while a large spout eye forms with a high gas flow rate, or no spout eye forms with a very small gas flow rate. Figure 8 displays the slag layer patterns with the gas flow rates of (a) 70 L/h and (b) 90 L/h, showing that a quite small eye is formed with the rate of 70 L/h while a large spout eye is formed with the rate of 90 L/h, and more large bubbles come out when the gas flow rate is higher. The gas flow rate of 70 L/h is a rate at which the spout eye appears to repetitively open and close according to the unsteady simulation results. Figure 9 shows a cycle of the slag eye open (Fig. 9a–c) and collapse (Fig. 9d–f) process both in experiment and

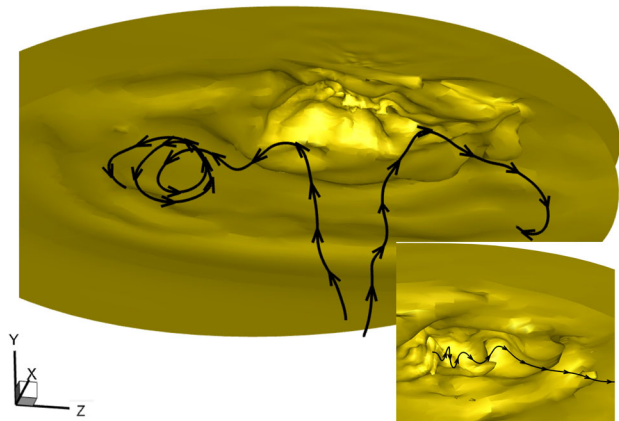


Fig. 10. Flow pattern underneath the slag layer.

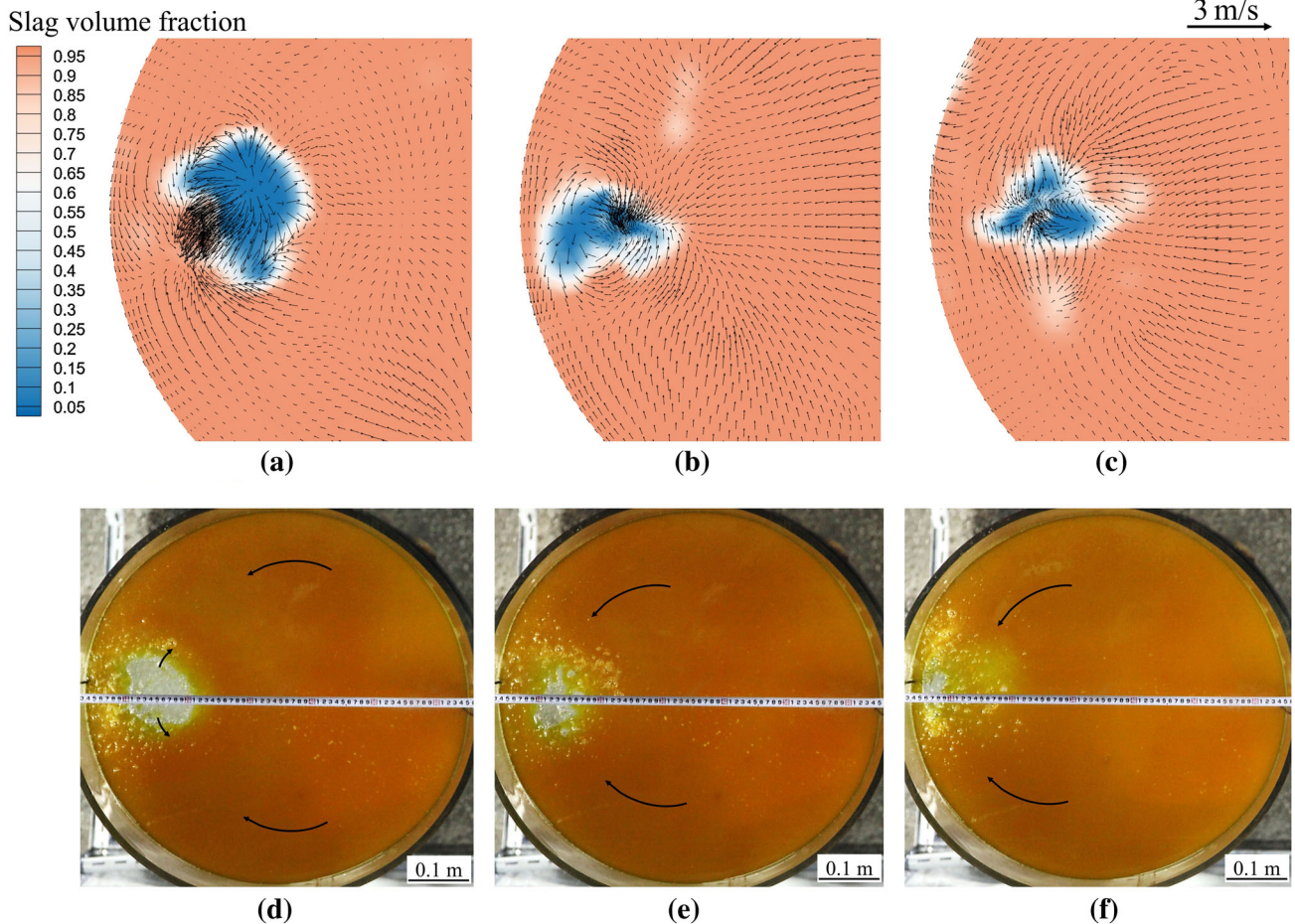


Fig. 11. Velocity inside the slag layer and the spout eye of (a–c) simulation and (d–f) experiment at different times.

simulation. Figure 9a shows the status when the eye is closed and the upwelling flow from the bubble plume is pushing the slag to the periphery of the ladle, and the spout eye grows to make the liquid under the slag layer exposed, as shown in Fig. 9c. After that, the spout eye starts to collapse as the slag goes to the spout eye center after the collision with the ladle wall and pushes the eye to close. Figure 9f shows the status when the eye is almost closed. Comparing the eye size between experiment and simulation, it also shows good agreement indicating that the present model can well predict the slag eye open–close process.

Figure 10 shows the flow pattern underneath the slag layer. The flow paths show two main flow directions. It is found that the bubbles drive the water to go upward, and then the water flows downward after the bubbles come out. The dispersed bubbles make turbulence and induce lots of multi-scale eddies which will cause the water–oil (liquid steel–slag) interface fluctuation and some other unsteady slag layer behaviors. As we know, the rotational flow near the interface may break the slag into quite small droplets and take them deep into the bath, which is the main inducement of slag inclusions and should be further understood. The enlarged picture shows a small rotational flow near the interface, which well reveals how the flow drags the oil down into the water.

Figure 11a–c displays the computed velocity and slag volume fraction near the top of the slag layer ($y = 0.74$ m) and Fig. 11d–f shows how the flow influences the slag eye formation. The blue color represents the water (liquid steel) and the pink represents the oil (slag). As the liquid underneath the slag layer always takes the slag to the periphery of the ladle, the slag on the top will go to the spout eye center to form a loop. The floating bubbles lead to the upwelling flow, and sometimes this is stronger than the flow to the eye center. Figure 11a shows the status when the upwelling flow is pushing the slag and the spout eye is growing. Figure 11b and c show the statuses when the upwelling flow is weak and the flow to the eye center is pushing the eye to close. Figure 11d–f are the observed statuses corresponding to the simulation results. The mechanism of slag eye open–close behavior is revealed via the analysis of the flow inside the slag layer.

CONCLUSION

A mathematical model based on the LES and the DPM–VOF coupled model is developed to simulate the multiphase bubbly flow in the gas–stirring ladle, and investigate the bubble–slag layer coupled behaviors. The bubbles are tracked using the DPM in a Lagrangian frame of reference, while the liquid steel, slag, and air phases are calculated using the VOF model in an Eulerian frame of reference. The

bubble coalescence is taken into account and the bubble diameter redistribution is calculated. Some conclusions can be drawn as follows:

1. The present model can factually predict the phenomena in the ladle metallurgy including the bubble transport, bubble diameter redistribution, slag layer fluctuation, slag droplet generation and the spout eye open–close process.
2. The eddies that are induced by the bubbles make the melt–slag interface fluctuate. The upwelling flow may break up the slag layer and the downward flow may drag slag droplets into the steel with the effect of shear stress. The present model provides a valid modeling framework for the slag entrainment investigation.
3. At a high gas flow rate, the interface fluctuates greatly and a quasi-steady state will be achieved to form a big spout eye. At a small gas flow rate, the slag eye opens and closes alternately, and the mechanism is revealed in the present work. The formed slag eye size of the present predictions qualitatively agrees well with the experiment.

ACKNOWLEDGEMENTS

Authors are grateful to the National Natural Science Foundation of China for support of this research, Grant No. 51574068.

REFERENCES

1. L. Nastac, *JOM* 56, 43 (2004).
2. Q. Zheng and A. Yu, *Phys. Rev. Lett.* 113, 068001 (2014).
3. L. Zhang, *Modell. Simul. Mater. Sci. Eng.* 8, 463 (2000).
4. A. Mukhopadhyay, E.W. Grald, K. Dhanasekharan, S. Sarkar, and J. Sanyal, *Steel Res. Int.* 76, 22 (2005).
5. B. Li, H. Yin, C. Zhou, and F. Tsukihashi, *ISIJ Int.* 48, 1704 (2008).
6. N. Kochi, Y. Ueda, T. Uemura, T. Ishii, and M. Iguchi, *ISIJ Int.* 51, 1011 (2011).
7. L. Li, Z. Liu, B. Li, H. Matsuura, and F. Tsukihashi, *ISIJ Int.* 55, 1337 (2015).
8. Z. Liu, L. Li, F. Qi, B. Li, M. Jiang, and F. Tsukihashi, *Metall. Mater. Trans. B* 46B, 406 (2015).
9. S.T. Johansen and F. Boysan, *Metall. Trans. B* 19B, 755 (1988).
10. D. Guo and G.A. Irons, *Metall. Mater. Trans. B* 31B, 1457 (2000).
11. H. Liu, Z. Qi, and M. Xu, *Steel Res. Int.* 82, 440 (2011).
12. L. Zhang, J. Aoki, and B.G. Thomas, *Metall. Mater. Trans. B* 37B, 361 (2006).
13. S.M. Cho, S.H. Kim, and B.G. Thomas, *ISIJ Int.* 54, 845 (2014).
14. K. Jin, B.G. Thomas, R. Liu, S.P. Vanka, and X.M. Ruan, *IOP Conf. Ser. Mater. Sci. Eng.* 84, 012095 (2015).
15. L. Li, Z. Liu, M. Cao, and B. Li, *JOM* 67, 1459 (2015).
16. J. Klostermann, K. Schaake, and R. Schwarze, *Int. J. Numer. Methods Fluids* 71, 960 (2013).
17. C.W. Hirt and B.D. Nichols, *J. Comput. Phys.* 39, 201 (1981).
18. L. Zhang, *JOM* 64, 1059 (2012).
19. Y.M. Lau, W. Bai, N.G. Deenn, and J.A.M. Kuipers, *Chem. Eng. Sci.* 108, 9 (2014).
20. D. Jain, J.A.M. Kuipers, and N.G. Deen, *Chem. Eng. Sci.* 119, 134 (2014).
21. T. Zhang, Z.G. Luo, C.L. Liu, H. Zhou, and Z.S. Zou, *Powder Technol.* 273, 154 (2015).

22. Z. Liu, B. Li, M. Jiang, and F. Tsukihashi, *ISIJ Int.* 53, 484 (2013).
23. M. van Sint Annaland, N.G. Deen, and J.A.M. Kuipers, *Chem. Eng. Sci.* 60, 2999 (2005).
24. J. Smagorinsky, *Month. Weather Rev.* 91, 99 (1963).
25. S.A. Morsi and A.J. Alexander, *J. Fluid Mech.* 55, 193 (1972).
26. A. Tomiyama, H. Tamai, I. Zun, and S. Hosokawa, *Chem. Eng. Sci.* 57, 1849 (2002).
27. D. Darmana, R.L.B. Henket, N.G. Deen, and J.A.M. Kuipers, *Chem. Eng. Sci.* 62, 2556 (2007).
28. P.J. O'Rourke, Collective drop effects on vaporizing liquid sprays, Ph.D Thesis, Princeton University, 1981.
29. A.A. Amsden, P.J. O'Rourke, and T.D. Butler, *NASA Sti/Recon Technical Report No.* 89, 1989.
30. X. Gu, S. Basu, and R. Kumar, *Int. J. Heat Mass Trans.* 55, 5322 (2012).